Microfluid Nanofluid (2008) 5:119–129
DOI 10.1007/s10404-007-0232-x

RESEARCH PAPER

Microfluidic analysis of CO_2 bubble dynamics using thermal lattice-Boltzmann method

K. Fei · W. H. Chen · C. W. Hong

Received: 17 August 2007 / Accepted: 10 October 2007 / Published online: 30 October 2007

Abstract By means of microfluidic analysis with a thermal lattice-Boltzmann method, we investigated the hydrophilic, thermal and geometric effects on the dynamics of CO_2 bubbles at anode microchannels (e.g., porous layers and flow channels) of a micro-direct methanol fuel cell. The simulation results show that a more hydrophilic wall provides an additional attractive force to the aqueous methanol in the flow direction and that moves the CO_2 bubble more easily. The bubble propagates quicker in the microchannel with a positive temperature gradient imposed from the inlet to the exit, mainly due to the Marangoni effect. Regarding the geometric effect of the microchannel, the bubble moves more rapidly in a divergent microchannel than in a straight or convergent channel. On the basis of the quantitative evaluation of hydrophilic, thermal and geometric effects, we are able to design the bubble-removal technique in micro fuel cells.

Keywords Thermal lattice-Boltzmann method · Bubble dynamics · Two-phase flow · Micro-direct methanol fuel cell

List of symbols

$\mathbf{e}$	lattice velocity vector
e	lattice speed (cm/s)
f	density distribution function (g/cm^3)
g	thermal distribution function (g K/cm^3)
$G^{\sigma\sigma'}$	interaction strength between the species σ and the other species σ' (cm^3/g s)
G^{σ}	fluid–solid interaction potential parameter of the species σ
G	gravitational constant (cm/s^2)
G'	non-dimensional constant
T	temperature (K)
t	time (s)
$\mathbf{U}$	velocity vector(u,v)
u	velocity in the x-direction (cm/s)
v	velocity in the y-direction (cm/s)
$\mathbf{X}$	position vector (x,y)

Greek symbols

β	thermal expansion coefficient (1/K)
ρ	density (g/cm^3)
θ	contact angle (°)
τ	collision time for momentum transfer
$\tau_{\mathbf{T}}$	collision time for energy transfer
ψ	function of the mass density

Subscripts

i	lattice velocity directions
∞	reference state

Superscripts

eq	equilibrium
σ	species

1 Introduction

Micro-direct methanol fuel cells (μDMFC) are considered a strong competitor of future power sources for portable equipment. The advantages are high efficiency, high power density, low operation temperature and almost zero pollution; but some technical challenges remain before commercialization is practicable. A major issue is the

K. Fei · W. H. Chen · C. W. Hong (✉)
Department of Power Mechanical Engineering,
National Tsing Hua University,
Hsinchu 30013, Taiwan
e-mail: cwhong@pme.nthu.edu.tw

removal of bubbles of carbon dioxide (CO_2) at the anode side, which are generated there on oxidation of methanol; these bubbles obstruct the diffusion layer and the flow channel if they are not removed efficiently, leading to μDMFC malfunction. The behavior of CO_2 bubbles at the anode has thus drawn much attention. One feasible way to investigate the bubble flow is through experimental flow visualization (Lu and Wang 2004; Yang et al. 2005; Wong et al. 2005). Most researchers focused on the bubble dynamics inside the flow channels of the fuel cell. The experimental approach is unable to provide detailed insight into the diffusion layer because of technical difficulties in performing that visualization. Computer simulation is thus an applicable approach to study bubble dynamics from a micro-scale viewpoint. We constructed mathematical models using a thermal lattice-Boltzmann method (TLBM) to observe the phenomenon of CO_2 bubbles in the anode microchannel of a μDMFC. The main focus of this research is on the thermal and geometric effects of the microchannel flow from a microfluidic viewpoint, the hydrophilic effect was inherited from the original lattice-Boltzmann method in our previous publications (Fei et al. 2006; Fei and Hong 2007).

The thermal effect influences the bubble transport significantly because the surface tension of a gas bubble depends on temperature. The temperature gradient around the gas bubble leads to a difference of surface tension around the bubble surface and causes a tangential force at the interface. The direction of the tangential force is opposite the temperature gradient, dragging the fluid around the bubble surface from a region of high temperature to a region of low temperature (Marangoni effect). A drag force exerts an opposite reaction on the bubble and makes it move from a cold region to a warm region. This phenomenon is evident when the size of the bubble is on a micro-scale and the temperature gradient is large. The movement of a bubble caused by a temperature gradient is known as thermocapillary motion and was first observed experimentally by Young et al. (1959). The Marangoni effect is a driving force of the bubble movement and has been widely utilized in the micro-flow device (Jun and Kim 1998; Takahashi et al. 1999, 2001). Although the lattice-Boltzmann method has undergone rapid progress in simulating multi-phase flow, little research has been conducted to discuss the dynamic distribution of temperature in a multi-phase flow including the thermal effect. Shan (1997) proposed a passive-scalar thermal lattice-Boltzmann model that treated temperature as a component of the mixture. Based on an analogy between mass and heat transfer, the temperature field was obtained on solving an additional equation similar to the original lattice-Boltzmann equation; compression work and viscous dissipation of heat were both neglected in this model. The momentum and energy equations were coupled by an external body force through the temperature gradient in the thermal lattice-Boltzmann equation. Yuan and Schaefer (2006a, b) combined this thermal lattice-Boltzmann model with a multi-phase flow model proposed by Shan and Chen (1993) to simulate the static distribution of temperature in a two-phase flow. Shi et al. (2004) derived a single-phase thermal lattice-Boltzmann model from the Boltzmann equation and the Maxwell–Boltzmann distribution, and obtained the model after applying the Bhatnagar–Gross–Krook (BGK) assumption. This model was capable of simulating the incompressible thermal flow with viscous heat dissipation and a large Prandtl number. Recently, Guo et al. (2007) developed another thermal lattice-Boltzmann for low Mach number flows from a two-relaxation-time kinetic model. They defined an additional distribution function to represent the total energy of the flow so that the compression work and viscous dissipation can easily be included in the model. In this paper, we derived a thermal lattice-Boltzmann model for a two-phase flow in the anode microchannel of methanol fuel cells. A simplified, 2D microchannel was set up in this research to mimic the real flow channel in a porous diffusion layer. Simulations were conducted by altering flow parameters one at a time to investigate the effects on the two-phase flow in the microchannel. Those parameters include the degree of hydrophilicity, the wall temperature distribution and the geometry of the microchannel. The main purpose is to investigate the bubble removal technique in the two-phase flow of gaseous CO_2 bubbles and the liquid of methanol–water solution.

2 Thermal lattice-Boltzmann method

Details of a 2D, nine-velocity (D2Q9) lattice-Boltzmann model for a two-phase flow, including the treatment of boundary conditions, were explicitly described in our previous work (Fei et al. 2006; Fei and Hong 2007). We derived the lattice-Boltzmann model from the physically-oriented concept proposed by Shan and Chen (1993). The main idea of this model was to treat additional effects of the two-phase flow as source terms of the momentum equation. In addition to the momentum equation, an energy equation is required to calculate the temperature field in this work. The thermal lattice-Boltzmann equation for heat transfer has a form identical to that of the previous lattice-Boltzmann equation and is expressed as

$$g_i(\mathbf{X}+\mathbf{e}_i\Delta t, t+\Delta t) - g_i(\mathbf{X}, t) = -\frac{1}{\tau_{\mathbf{T}}}\left[g_i(\mathbf{X}, t) - g_i^{(\mathrm{eq})}(\mathbf{X}, t)\right] \tag{1}$$

in which g_i ($\mathbf{X}$, t) is the thermal distribution function that is a function of space $\mathbf{X}$, and time, t; $\mathbf{e}_i$ lattice velocity vector

in the i direction; $\tau_{\mathbf{T}}$ dimensionless collision time for heat transfer; and the superscript eq denotes an equilibrium state. The mathematical form of the thermal equilibrium distribution functions in each direction, $g_i^{(\mathrm{eq})}$, was derived by Shi et al. (2004) as the general equation of

$$g_i^{(\mathrm{eq})} = w_i \rho T \left[1 + 3\,\frac{\mathbf{e}_i \cdot \mathbf{U}}{e^2} + \frac{9}{2}\,\frac{(\mathbf{e}_i \cdot \mathbf{U})^2}{e^4} - \frac{3}{2}\,\frac{(\mathbf{U} \cdot \mathbf{U})}{e^2} \right] \tag{2}$$

in which $w_i = 4/9$ for $i = 0$, $w_i = 1/9$ for $i = 1 - 4$ and $w_i = 1/36$ for $i = 5 - 8$; $\mathbf{U}$ is the particle velocity vector that includes the velocity components in both x and y directions; ρ is the density at a certain position in the flow field. The thermal energy density is defined as the sum over the thermal distribution functions and is expressible as

$$\rho^{\sigma}(\mathbf{X},\ t) T^{\sigma}(\mathbf{X},\ t) = \sum_i g_i^{\sigma}(\mathbf{X},\ t) \tag{3}$$

where superscript σ denotes the species, σ. The temperature of each species $T^{\sigma}(\mathbf{X}, t)$, can be calculated from the thermal energy density divided by the mass density $\rho^{\sigma}(\mathbf{X}, t)$.

The fluid density can be approximated as an inversely linear function to the temperature over a small temperature range. In our case of the μDMFC, the operation range is from 298 to 333 K. The additional thermal force caused by the density difference due to the temperature variation is

$$F^{\sigma}_{\mathrm{thermal}}(\mathbf{X},\ t) = \tau_{\mathbf{T}} \left[\rho^{\sigma}_{\infty}(\mathbf{X},\ t) \beta^{\sigma} \mathbf{G} (T^{\sigma} - T^{\sigma}_{\infty}) \right] \tag{4}$$

in which β^{σ} is the thermal expansion coefficient of species σ; $\mathbf{G}$ is the gravitational constant; ρ_{∞} and T_{∞} are the reference density and temperature, respectively. This additional force can be added to the original source term of the momentum equation which includes the surface tension, the fluid–solid wall interaction and the buoyancy force. The new general momentum equation is expressed as

$$\rho^{\sigma}(\mathbf{X},\ t) \mathbf{U}^{\sigma}(\mathbf{X},\ t) = \sum_i f_i^{\sigma}(\mathbf{X},\ t) \mathbf{e}_i + F^{\sigma}_{\mathrm{total}}(\mathbf{X},\ t) \tag{5}$$

in which f is the mass density distribution function and the total source term is

$$\begin{aligned} F^{\sigma}_{\mathrm{total}}(\mathbf{X},\ t) &= F^{\sigma}_{\mathrm{surface\ tension}}(\mathbf{X},\ t) + F^{\sigma}_{\mathrm{solid}}(\mathbf{X},\ t) \\ &+ F^{\sigma}_{\mathrm{buoyancy}}(\mathbf{X},\ t) + F^{\sigma}_{\mathrm{thermal}}(\mathbf{X},\ t) \end{aligned} \tag{6}$$

Each external force, except the thermal force in Eq. (4), is expressible as

$$\begin{aligned} &F^{\sigma}_{\mathrm{surface\ tension}}(\mathbf{X},\ t) \\ &= -\tau^{\sigma} \left[\psi^{\sigma}(\mathbf{X},\ t) \sum_{\sigma'} G^{\sigma\sigma'} \sum_i \psi^{\sigma'}(\mathbf{X} + \mathbf{e}_i \Delta t,\ t) \mathbf{e}_i \right] \end{aligned} \tag{7}$$

$$F^{\sigma}_{\mathrm{solid}}(\mathbf{X},\ t) = -\rho^{\sigma}(\mathbf{X},\ t) \sum_i G^{\sigma}_i s(\mathbf{X} + \mathbf{e}_i \Delta t) \mathbf{e}_i \tag{8}$$

$$F^{\sigma}_{\mathrm{buoyancy}}(\mathbf{X},\ t) = G' \sum_i \rho^{\sigma}(\mathbf{X} + \mathbf{e}_i \Delta t,\ t) \mathbf{e}_i \tag{9}$$

In the above equations, $\psi^{\sigma}(\mathbf{X}, t)$ is a function of the mass density of species σ at position vector $\mathbf{X}$; $G^{\sigma\sigma'}$ represents the strength of the interaction between different species and is set constant for simplicity; τ^{σ} is the collision time of the species σ for momentum transfer; G^{σ} is a fluid–solid interaction potential parameter; s is a function of particle position ($s = 0$ when the particle is in the fluid, $s = 1$ when the particle is at the fluid/solid interface); G' is a non-dimensional constant. Shan and Chen (1994) suggested that the form of $\psi^{\sigma}(\mathbf{X}, t)$ can be represented by

$$\psi^{\sigma}(\mathbf{X},\ t) = A \exp(-\rho_{\infty}/\rho) \tag{10}$$

in which A is a constant and is set to be 5.4 in the following simulations.

3 Boundary conditions for TLBM

To determine the unknown thermal distribution functions at the boundary nodes, thermal boundary equations were derived following the principle given by Inamuro et al. (2002). Figure 1 shows the known and unknown thermal distribution functions at the inlet, exit, upper and lower walls of the microchannel.

3.1 Inlet and exit boundaries

Assuming the inlet flow temperature T_{in}, to be known at the boundary node, the energy equation in the TLBM is

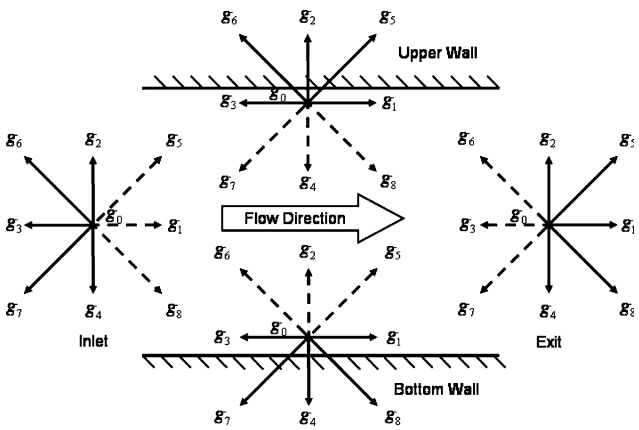

Fig. 1 Thermal distribution functions, g, ($i = 0 - 8$), at boundaries of a microchannel; *solid lines* are known conditions and *dashed lines* are unknown ones

$$\rho T_{\text{in}} = \sum_i g_i \tag{11}$$

The summation of the unknown thermal distribution functions is expressible as

$$g_1 + g_5 + g_8 = \frac{1}{6}\rho T' \left[1 + 3\frac{u}{e} + 3\frac{u^2}{e^2}\right] \tag{12}$$

in which T' is the unknown temperature. Substituting Eq. (11) into Eq. (12), the unknown temperature, T', is obtained as

$$T' = \frac{6}{\rho\left[1 + 3\left(\frac{u}{e}\right) + 3\left(\frac{u^2}{e^2}\right)\right]}\left[\rho T_{\text{in}} - g_0 - g_2 - g_3 - g_4 - g_6 - g_7\right] \tag{13}$$

Those unknown thermal distribution functions of the inlet nodes are

$$g_1 = \frac{1}{9}\rho T' \left[1 + 3\frac{\mathbf{e}_1 \cdot \mathbf{U}}{e^2} + \frac{9}{2}\frac{(\mathbf{e}_1 \cdot \mathbf{U})^2}{e^4} - \frac{3}{2}\frac{\mathbf{U}^2}{e^2}\right] \tag{14}$$

$$g_5 = \frac{1}{36}\rho T' \left[1 + 3\frac{\mathbf{e}_5 \cdot \mathbf{U}}{e^2} + \frac{9}{2}\frac{(\mathbf{e}_5 \cdot \mathbf{U})^2}{e^4} - \frac{3}{2}\frac{\mathbf{U}^2}{e^2}\right] \tag{15}$$

$$g_8 = \frac{1}{36}\rho T' \left[1 + 3\frac{\mathbf{e}_8 \cdot \mathbf{U}}{e^2} + \frac{9}{2}\frac{(\mathbf{e}_8 \cdot \mathbf{U})^2}{e^4} - \frac{3}{2}\frac{\mathbf{U}^2}{e^2}\right] \tag{16}$$

The unknown distribution functions at the exit boundary, g_3, g_6 and g_7, can also be determined with the similar procedure as above.

3.2 Wall boundaries

In Fig. 1, those unknown thermal distribution functions of the boundary nodes at the bottom wall are obtainable with a similar procedure and are expressed as

$$g_2 = \frac{1}{9}\rho T'(\mathbf{X}) \left[1 + 3\frac{\mathbf{e}_2 \cdot \mathbf{U}}{e^2} + \frac{9}{2}\frac{(\mathbf{e}_2 \cdot \mathbf{U})^2}{e^4} - \frac{3}{2}\frac{\mathbf{U}^2}{e^2}\right] \tag{17}$$

$$g_5 = \frac{1}{36}\rho T'(\mathbf{X}) \left[1 + 3\frac{\mathbf{e}_5 \cdot \mathbf{U}}{e^2} + \frac{9}{2}\frac{(\mathbf{e}_5 \cdot \mathbf{U})^2}{e^4} - \frac{3}{2}\frac{\mathbf{U}^2}{e^2}\right] \tag{18}$$

$$g_6 = \frac{1}{36}\rho T'(\mathbf{X}) \left[1 + 3\frac{\mathbf{e}_6 \cdot \mathbf{U}}{e^2} + \frac{9}{2}\frac{(\mathbf{e}_6 \cdot \mathbf{U})^2}{e^4} - \frac{3}{2}\frac{\mathbf{U}^2}{e^2}\right] \tag{19}$$

in which the unknown temperature $T'(\mathbf{X})$ is

$$T'(\mathbf{X}) = \frac{6}{\rho\left[1 + 3\left(\frac{v}{e}\right) + 3\left(\frac{v^2}{e^2}\right)\right]} \left[\rho T_{\text{wall}}(\mathbf{X}) - g_0 - g_1 - g_3 - g_4 - g_7 - g_8\right] \tag{20}$$

The wall temperature, $T_{\text{wall}}(\mathbf{X})$, is a function of the node position along the wall or it can be a constant wall temperature. The effect of wall temperature on the flow can be investigated in the following section. The unknown distribution functions of the upper wall can also be expressed in a similar way as above, except that g_4, g_7 and g_8 are unknowns.

4 Simulation results

The example simulation domain in our case is a straight microchannel of height 1.5 μm representing the pore diameter of a diffusion layer and length 15.9 μm, which is ten times the height to make the 2D assumption valid (as shown in Fig. 2a). Figure 2b is the grid generation of the D2Q9 TLBM model, in which Δx and Δy are both set to be 0.05 μm. There are in total 9,540 grid cells in the example simulation case.

4.1 Effect of hydrophilicity

The hydrophilicity between the fluid and the wall surface is controlled by adjusting the value of the fluid–solid interaction potential parameter, G^σ in Eq. (8), in this simulation. A larger value of G^σ implies the microchannel wall to be less hydrophilic. Physically, the degree of hydrophilicity can be represented by the contact angle in the two-phase flow. The definition of the contact angle of the bubble in a microchannel is defined as the angle between the solid wall and the line tangent to the bubble surface at the contact edge, as shown in Fig. 3a. The total surface energy E_s of the 2D two-phase flow in the microchannel is expressed as

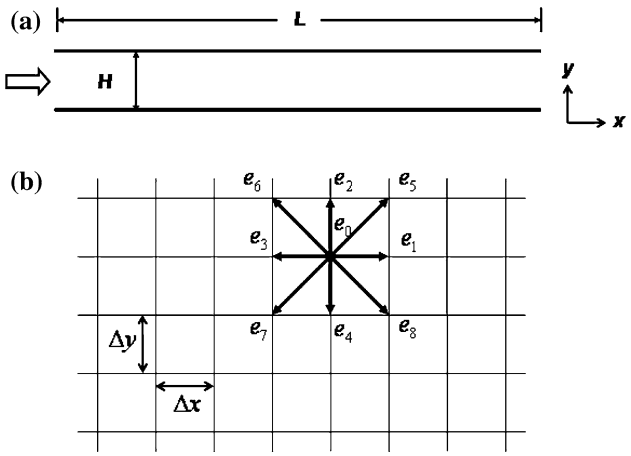

Fig. 2 **a** Simulation domain (e.g., length L = 15.9 μm, height H = 1.5 μm) of a straight horizontal microchannel representing the flow path of the diffusion layer and the flow channel; **b** grid generation of the D2Q9 model ($\Delta x = \Delta y$ = 0.05 μm), the total number of grid cells is 9,540

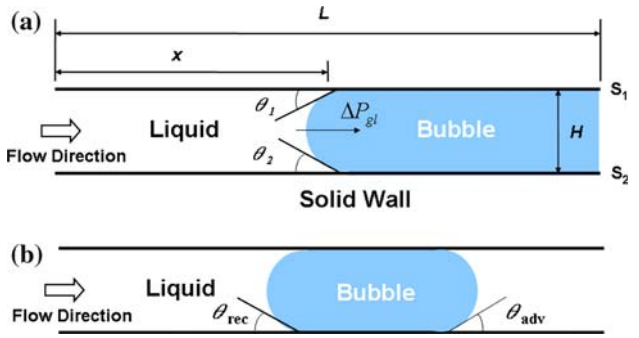

Fig. 3 **a** Diagram of the contact angle definition of bubble flow in a microchannel (ΔP_{gl} forward pressure drop across the gas–liquid interface; L length of the microchannel; H height of the horizontal microchannel; S_1 upper surface of the microchannel; S_2 lower surface of the microchannel; x length of the liquid phase; θ_1 upper contact angle; θ_2 lower contact angle); **b** illustration of a moving bubble in the microchannel (θ_{rec} the receding contact angle; θ_{adv} the advancing contact angle)

$$E_s = x\gamma_{S_1 l} + x\gamma_{S_2 l} + (L-x)\gamma_{S_1 g} + (L-x)\gamma_{S_2 g} \tag{21}$$

in which x is the length of the liquid phase, L length of the microchannel, $\gamma_{S_i j}$ (i = 1, 2; j = g, l) is the solid–liquid or solid–gas surface energy of the upper wall S_1, and the lower wall S_2 (see Fig. 3a). Young's equation (Young 1805) describes the relation between the surface energy and the contact angle θ,

$$\gamma_{sg} = \gamma_{sl} + \gamma_{gl}\cos\theta, \tag{22}$$

where γ_{sg}, γ_{sl} and γ_{gl} are the solid–gas, solid–liquid and gas–liquid surface energies, respectively. After substituting Eq. (22) into Eq. (21) and differentiating with respect to the variable x, the forward pressure drop across the gas–liquid interface acting on the rear of the bubble ΔP_{gl}, is obtained as

$$\Delta P_{gl} = \frac{\gamma_{gl}}{H}(\cos\theta_1 + \cos\theta_2) \tag{23}$$

in which H is the height of the horizontal microchannel; θ_1 is the upper contact angle and θ_2 is the lower contact angle. The pressure drop across the gas–liquid interface evidently depends on the contact angles (or the hydrophilicity at the upper and lower walls), the gas–liquid surface tension and the channel width. When a bubble moves in a microchannel, as illustrated in Fig. 3b, an advancing contact angle is formed at the front contact edge between the bubble surface and the channel wall, while a receding contact angle is formed at the rear contact edge. The advancing contact angle may be different from the receding contact angle depending on flow conditions and surface property at the solid wall. According to the above analysis, when the advancing contact angle of the moving bubble is smaller than the receding contact angle, the bubble sustains a larger backward pressure drop than the forward pressure drop; the transport of the bubble is thus obstructed.

To study the effect of the hydrophilicity, we chose a set of G^σ values from –0.007 to 0.007 in the step of 0.001, which are related to the contact angle as shown in Fig. 4. These G^σ values and other flow parameters used in the simulations are listed in Table 1. In Fig. 4, the contact angle of the bubble increases from 10.0° to 51.0° with G^σ increasing from –0.007 to 0.007, indicating that the larger the value of G^σ, the greater the contact angle, the less the hydrophilicity. The velocity of the bubble movement in the microchannel also varies with hydrophilicity. The bubble velocity is calculated on recording the traveling distance of the bubble center during a certain interval. When the channel wall is hydrophilic, the wall provides an attractive force on the liquid, making the liquid flow more rapidly than in a less hydrophilic microchannel. The bubble movement in the liquid is likewise affected; it transports with greater velocity if the liquid flows more rapidly. In addition, the pressure drop across the gas–liquid interface, ΔP_{gl}, increases if the microchannel is more hydrophilic (Eq. 23). The CO_2 bubble in a hydrophilic microchannel is thus able to transport more rapidly than in a hydrophobic microchannel, as indicated by Fig. 4. The first conclusion to be drawn here is that a hydrophilic microchannel is preferable for the purpose of bubble removal at the anode of the μDMFC.

Further analysis regarding the effect of hydrophilicity is conducted on imposing a linear gradient of hydrophilicity on both walls of the microchannel. From the previous results, the bubble velocity is 280.2 μm/s when the contact angle is 10.0° (G^σ = –0.007), and the velocity is 266.9 μm/

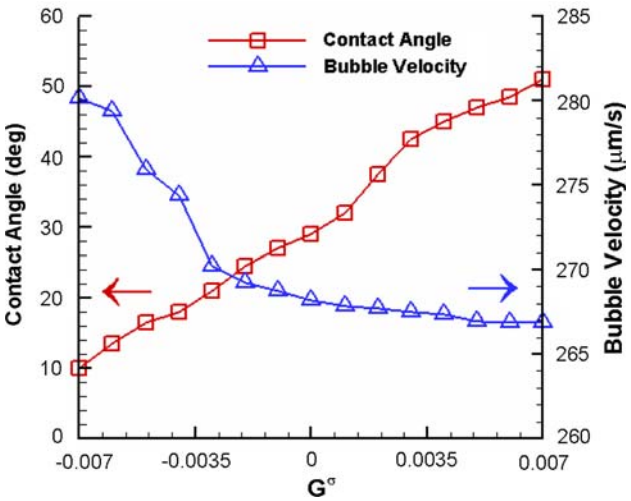

Fig. 4 Contact angle and bubble velocity versus the varied value of the fluid–solid interaction strength G^σ. The *diagram* indicates that the larger the value of G^σ, the greater the contact angle, the less the hydrophilicity is, and the lower the bubble transport velocity

Table 1 Input parameters for the simulation with varied hydrophilicity

Parameter	Variable	Value
Temperature	T (K)	333
Channel length	L (μm)	15.9
Channel height	H (μm)	1.5
Inflow velocity	U (μm/s)	250
Interaction strength between fluid species	$G^{\sigma\sigma'}(cm^3/g.s)$	3.72
Fluid–solid interaction strength	G^{σ}	–0.007, –0.006, –0.005, –0.004, –0.003, –0.002, –0.001, 0, 0.001, 0.002, 0.003, 0.004, 0.005, 0.006, 0.007
Linear gradient of the fluid–solid interaction strength	G^{σ}	0.007 → –0.007 –0.007 → 0.007

The fluid–solid interaction strength, G^{σ} varies from –0.007 to 0.007 in the step of 0.001. A larger G^{σ} implies the microchannel wall to be less hydrophilic

s when the microchannel is less hydrophilic (G^{σ} = 0.007). If we impose a linear gradient of hydrophilicity along both walls from G^{σ} = 0.007 to –0.007 (51.0° to 10.0° in contact angle), the average bubble velocity becomes 262.7 μm/s, which is much smaller than the previous two cases. With a positive gradient of hydrophilicity, the advancing contact angle of the moving bubble is invariably smaller than the receding contact angle (Fig. 5a). The backward pressure drop acting on the front of the bubble is then larger than the forward pressure acting on the rear of the bubble, causing the bubble velocity to decrease. In addition, when the contact angle is varied from 10.0° to 51.0° (G^{σ} = –0.007 → 0.007), the hydrophilicity decreases along the wall; the average bubble velocity is 274.3 μm/s. Figure 5b shows that the difference between the advancing and receding contact angles of the bubble is imperceptible in this case. The effect of the pressure drop is insignificant compared with the effect of the hydrophobic nature of the microchannel. The bubble velocity is hence smaller than in the case of a hydrophilic microchannel (contact angle = 10.0°). A comparison of bubble transport velocity among the above four cases is illustrated in Fig. 6. The bubble clearly moves most rapidly in the hydrophilic microchannel with a contact angle fixed at 10.0° (case 1). When the contact angle is decreased from 51.0° to 10.0° along the flow direction, it is most unfavorable for the bubble transport (case 4).

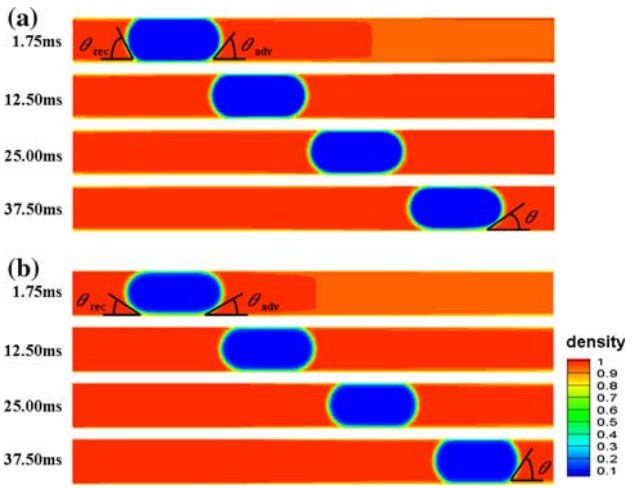

Fig. 5 Density field diagram of the bubble flow at each instant in a microchannel with varied hydrophilicity: **a** contact angle θ, varied from 51.0° to 10.0° along the flow direction and $\theta_{adv} < \theta_{rec}$; **b** contact angle varied from 10.0° to 51.0° and $\theta_{adv} > \theta_{rec}$ (inflow velocity is fixed at 250 μm/s)

4.2 Thermal effect

The temperature field in a microchannel plays an important role in the bubble dynamics of the μDMFC. This is due to

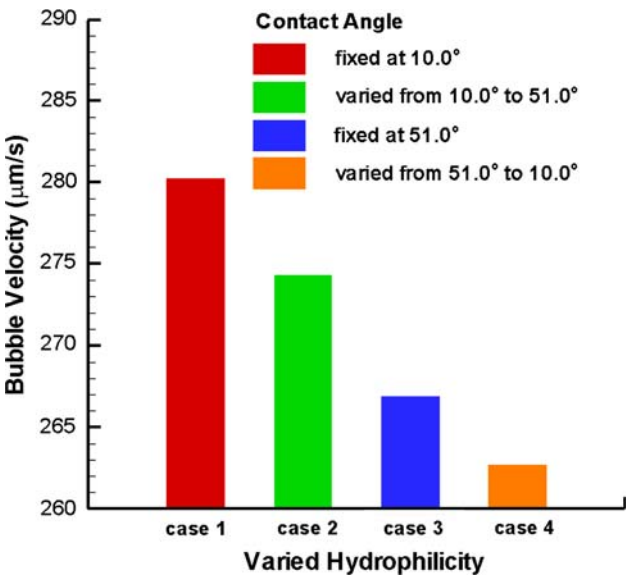

Fig. 6 Bubble transport velocity of four cases with varied hydrophilicity at the microchannel wall (case 1 contact angle fixed at 10.0°; case 2 contact angle varied from 10.0° to 51.0° linearly from inlet to exit; case 3 contact angle fixed at 51.0°; case 4 contact angle varied from 51.0° to 10.0° linearly from inlet to exit)

Table 2 Experimental result of surface tension of a 2 M methanol–water solution versus the solution temperature; the higher the temperature, the smaller the surface tension

Temperature (K)	298	303	308	313	318	323
Surface tension ($\times 10^3$ N/m)	55.16	54.62	54.06	53.29	52.66	52.01

the fact that the surface tension of the methanol–water solution varies with temperature (Table 2) such that the surface tension decreases from the magnitude of 55,000 to 52,000 N/m when the solution temperature increases from 298 to 323 K. The surface tension in our simulation is controlled by the parameter for the interaction strength between two species, $G^{\sigma\sigma'}$, in Eq. (7). It is necessary to ascertain the relation between the surface tension of the methanol–water solution and its corresponding value of $G^{\sigma\sigma'}$ at varied temperature. Figure 7 shows that the parameter $G^{\sigma\sigma'}$ at a particular temperature, required in the simulation, is readily obtained through a linear relationship with respect to the surface tension and the solution temperature. The surface tension is also inversely linear to the temperature as indicated in Table 2. Table 3 shows those input parameters in the simulation with solution temperature variation. The fluid–solid interaction strength is here set to be –0.004, i.e. contact angle = 18.0° as the base case. The temperature range used in the simulation is from 298 to 333 K according to the operation range of the μDMFC. The thermal effects on the bubble dynamics are shown in Fig. 8. The temperature field of the microchannel is assumed to be uniform in the beginning cases. With the preset temperature of the flow field increasing from 298 to 333 K, the surface tension of the methanol–water solution decreases. The bubble volume in the microchannel that the surface tension can support is thus reduced. The length of the plug bubble is decreased from 76.4 to 67.4 μm, which is defined as the distance between the front and the rear of the slug. The water–methanol solution flows into the microchannel with a constant velocity (250 μm/s). The bubble velocity is affected also by the temperature of the

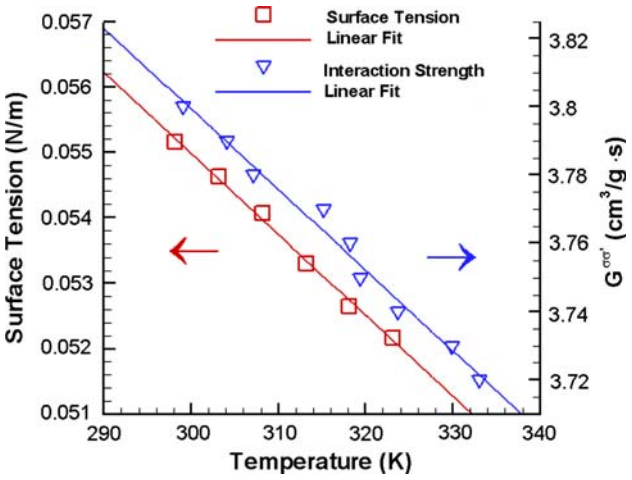

Fig. 7 Surface tension of methanol–water solution (2 M) and its corresponding $G^{\sigma\sigma'}$ value at varied temperature; they are curve fitted linearly in our simulation

flow field. As shown in Fig. 8, the bubble velocity increases from 270.1 to 280.2 μm/s when the preset temperature of the flow field varies from 298 to 333 K, because the mobility of a bubble is increased with a decreased size of the slug. A second conclusion is thus that a higher temperature is favorable for bubble transport.

As mentioned previously, the bubble moves from a region of low temperature to that of high temperature spontaneously due to the Marangoni effect. Figure 9 reveals the bubble velocity in a microchannel under various velocities of inlet flow. The temperature is 298 K at the inlet and 333 K at the outlet. A linear gradient from 298 to 333 K is imposed along both channel walls. The figure illustrates that, when the inlet flow velocity is zero, the bubble transports with a velocity 50.0 μm/s rather than remaining at its original position. The reason is that the temperature gradient around the gas bubble causes a tangential force opposite to the temperature gradient, dragging the fluid around the bubble surface from a region of high temperature to that of low temperature. The reaction force makes the bubble move in the opposite direction even

Table 3 Input parameter variation for the simulation with varied temperature distribution of a microchannel; the interaction strength between fluid species, $G^{\sigma\sigma'}$, varies with solution temperature inversely

Parameter	Variable	Value
Temperature	T (K)	298, 303, 308, 313, 318, 323, 328, 333
Channel length	L (μm)	15.9
Channel height	H (μm)	1.5
Inflow velocity	U (μm/s)	250
Fluid–solid interaction strength	G^{σ}	–0.004
Interaction strength between fluid species	$G^{\sigma\sigma'}(cm^3/g.s)$	3.80, 3.79, 3.78, 3.77, 3.76, 3.74, 3.73, 3.72 corresponding to the above temperatures

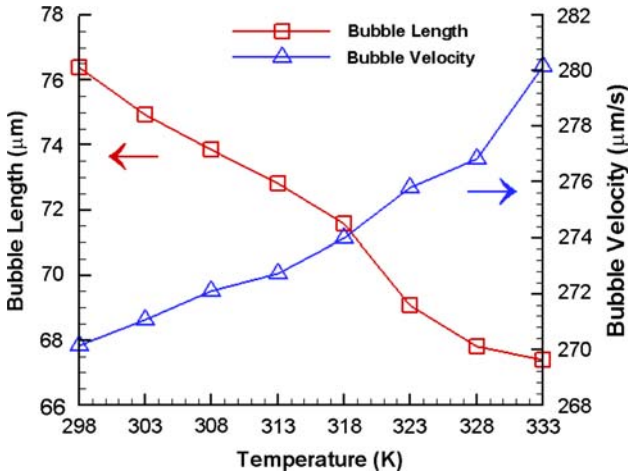

Fig. 8 Bubble length and bubble velocity at varied flow temperature (inlet flow velocity 250 μm/s)

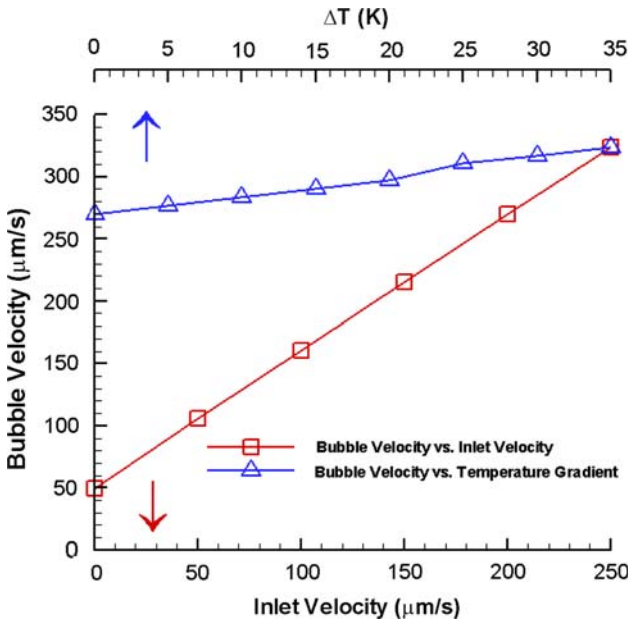

Fig. 9 Bubble transport velocity versus inlet velocity and the wall temperature difference. The *square symbols* show bubble velocity versus varied inlet velocity from 0 to 250 μm/s (wall temperature difference ΔT is fixed at 35 K, from 298 K at the inlet to 333 K at the exit); the *triangular symbols* show the relation between the bubble velocity and the wall temperature difference (inlet velocity is fixed at 250 μm/s)

without an inlet flow velocity. Figure 9 shows that the bubble velocity increases linearly with inlet flow velocity because of increased inlet flow momentum. The driving force for bubble transport through the Marangoni effect also increases with the temperature gradient. Hence a bubble moves more rapidly in a flow field with a large temperature gradient. Other simulations are conducted by altering the wall temperature of the outlet from 298 to

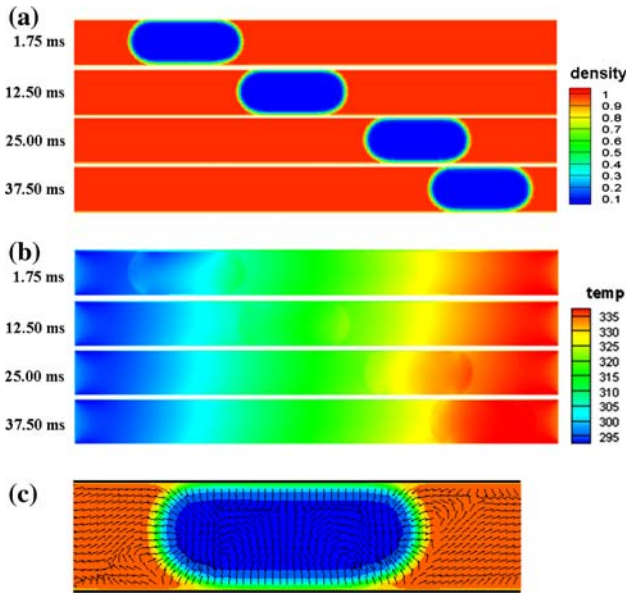

Fig. 10 **a** Density field diagram at each instant of the bubble flow in the microchannel (0.1 – 1.0 g/cm^3); **b** corresponding temperature distribution diagram (simulation conditions are set at inlet velocity: 250 μm/s; inlet temperature 298 K; outlet temperature 333 K; the wall temperature varies from 298 to 333 K linearly from the inlet to the exit); **c** an enlarged view of the velocity vectors superimposed on the bubble density diagram

333 K, while the temperature and velocity of the inlet are fixed at 298 K and 250 μm/s. Varied linear wall temperature gradients are imposed on the walls along the flow direction according to the temperature at the outlet. The relation between bubble velocity and the temperature gradient is illustrated in Fig. 9. An increased temperature gradient is clearly responsible for an increasing mobility of the bubble.

The density and temperature distribution of the bubble flow in the microchannel with elapsed time are presented in Fig. 10a and b, respectively. In the figure, the inlet velocity and temperature is maintained at 250 μm/s and 298 K; the temperature at the outlet is 333 K, so that the wall temperature distribution is imposed as ΔT = 35 K in the flow direction. The length of the bubble gradually decreases as it transports along the microchannel (Fig. 10a). When the bubble moves from a region of low temperature to that of high temperature, the surface tension decreases with increasing temperature. The length of the bubble slightly decreases through the variation of surface tension with temperature. The temperature distribution of the flow field in the microchannel is shown in Fig. 10b. The flow temperature is evenly distributed and increases along the direction of an imposed wall temperature gradient, mainly because the effect of conduction is dominant relative to convection for micro-scale heat transfer. Only a small temperature difference exists near the bubble surface as the

density is discontinuous across the surface. Figure 10c shows an enlarged view of the velocity vector diagram superimposed on the density field. The illustration indicates that the velocity fields inside the bubble and outside the bubble have their own flow patterns. There are two vortexes inside the CO_2 bubble, one clockwise, and the other counter-clockwise. The methanol fluid flow directions outside the bubble are mainly forward, although some reversed flow may happen near the bubble surface. The bubble velocity in this case (ΔT = 35 K) is 323.9 μm/s. If a negative wall temperature gradient (from 333 to 298 K) is applied, the bubble velocity is greatly decreased to 221.8 μm/s. The driving force of the bubble movement through the Marangoni effect is in the opposite direction of the inlet flow, causing the decrease of the bubble velocity. Figure 11 compares the bubble velocity in four cases of wall temperature at 298, 333, ΔT = 35 K (from 298 to 333 K) and ΔT = –35 K (from 333 to 298 K). The positive wall temperature gradient is obviously favorable for bubble transport because of the assistance of the Marangoni effect.

4.3 Geometric effect

The bubble transport is affected also by the shape of a microchannel. The geometric effect is investigated with designs of three kinds—convergent, straight and divergent microchannels. The flow temperature is first fixed at 333 K for those three cases. In further analysis, wall temperature distributions of four cases discussed in the preceding section are imposed on the microchannels to observe the variation of the bubble flow in each case. The parametric variables are explicitly listed in Table 4. Figure 12a and b compare the bubble flow phenomenon between a convergent and a divergent microchannel with the same flow temperature (333 K). When the bubble travels in a convergent channel, the bubble is gradually compressed as it moves toward the outlet and the bubble length is increased (Fig. 12a). The capillary force also increases along the flow direction as the height of the convergent microchannel decreases. The bubble flow is thus obstructed because of an increasing capillary force, and the bubble tends to block a convergent microchannel. The bubble flow in a divergent microchannel is shown in Fig. 12b. The bubble length is decreasing because the height of the channel is gradually increasing. The capillary force is decreasing along the flow direction of a divergent microchannel, making the bubble move more rapidly than in a convergent microchannel. The calculated bubble velocities are 267.9 and 281.3 μm/s in convergent and divergent microchannels, respectively. When the flow temperature is set to be 298 K, the bubble velocity is decreased to 262.0 μm/s in a convergent microchannel whereas it is 276.9 μm/s in a divergent microchannel.

As described previously, a positive temperature gradient is helpful for bubble transport. The Marangoni effect

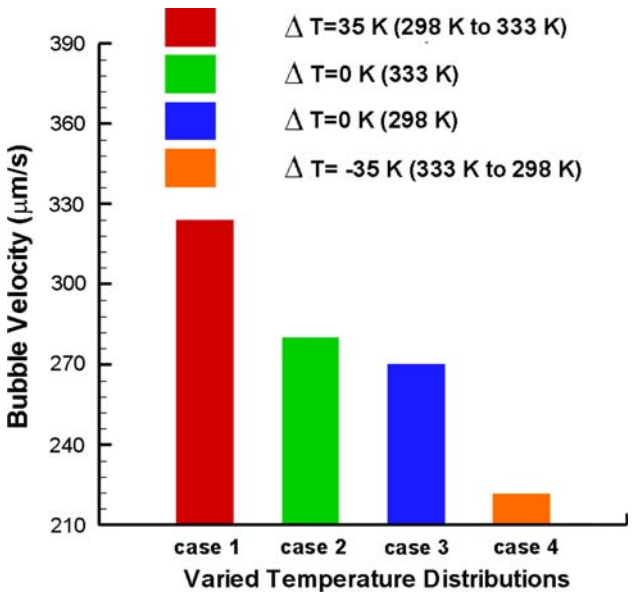

Fig. 11 Bubble transport velocity of four cases with varied wall temperature distributions of the microchannel (case 1 temperature varied from 298 to 333 K linearly from inlet to exit; case 2 temperature kept at 333 K; case 3 temperature kept at 298 K; case 4 temperature varied from 333 to 298 K linearly from inlet to exit)

Table 4 Parameter variation for the simulation with varied geometry and temperature distribution of a microchannel

Parameter	Variable		Value
Temperature	T (K)		298, 333
Channel length	L (μm)		15.9
Channel height[a]	Convergent	H_{in} (μm)	2.0
		H_{out} (μm)	1.0
	Divergent	H_{in} (μm)	1.0
		H_{out} (μm)	2.0
	Straight	H (μm)	1.5
Inflow velocity[b]	Convergent	U (μm/s)	187.5
	Divergent	U (μm/s)	375
	Straight	U (μm/s)	250
Fluid–solid interaction strength	G^{σ}		–0.004
Interaction strength between fluid species	$G^{\sigma\sigma'}$ (cm^3/g s)		3.80 (298 K), 3.72 (333 K)

[a] H_{in} and H_{out} are the heights of the inlet and outlet, respectively, of the non-straight channel

[b] Inlet velocities are varied for convergent, divergent and straight channels to ensure that the inlet volume flow rate is a constant

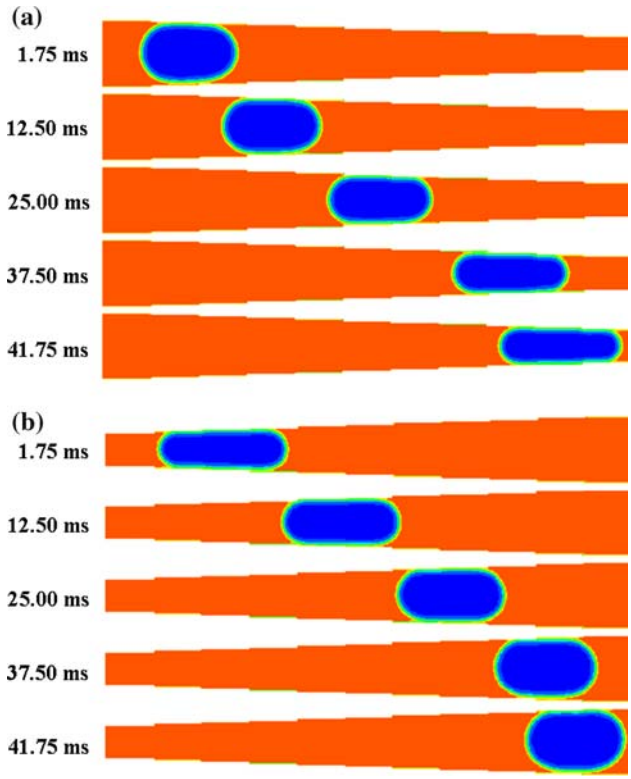

Fig. 12 Bubble flow in a (**a**) convergent microchannel and (**b**) divergent microchannel (inlet flow rate is fixed at 375 $\mu m^2/s$; both flow and wall temperatures are kept at 333 K)

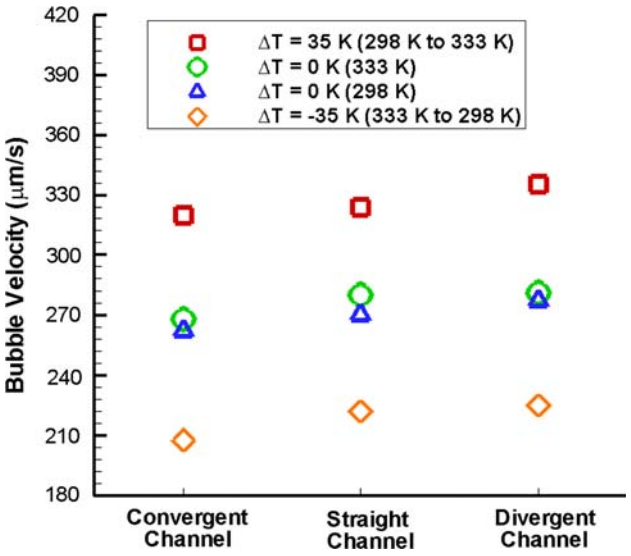

Fig. 13 Bubble transport velocity in convergent, straight and divergent microchannels with varied wall temperature distribution (*square symbols* temperature varied from 298 to 333 K linearly from inlet to exit; *circular symbols* temperature kept at 333 K; *triangular symbols* temperature kept at 298 K; *diamond symbols* temperature varied from 333 to 298 K linearly from inlet to exit)

makes a bubble move more rapidly with a positive temperature gradient than with a uniform temperature distribution. The bubble velocities are 319.6 and 335.3 μm/s in convergent and divergent channels, respectively, with a wall temperature gradient from 298 to 333 K. Besides, if the wall temperature gradient is from 333 to 298 K, the bubble velocity decreases greatly –207.6 μm/s in a convergent microchannel and 225.1 μm/s in a divergent microchannel. The bubble velocities in microchannels with varied geometries and temperature distributions are compared in Fig. 13. The divergent microchannel is favorable for the movement of a bubble because of the decreasing capillary force. The bubble velocity also greatly increases if a positive wall temperature gradient is imposed on a channel. A divergent channel with a positive wall temperature gradient is hence most favorable for bubble transport in the microchannel.

5 Conclusions

Using thermal lattice-Boltzmann approach, we investigated the hydrophilicity, thermal and geometric effects on bubble dynamics in a microchannel. The simulation results show that a hydrophilic microchannel is preferable for bubble transport over a hydrophobic microchannel. The bubble velocity increases with increasing hydrophilicity of a microchannel, mainly because a hydrophilic wall provides an attractive force on the liquid, making the bubble move easily in the hydrophilic microchannel. The pressure drop across a gas–liquid interface is also increased with hydrophilicity. A bubble hence travels more readily in a more hydrophilic microchannel than in a less hydrophilic microchannel. If a linear gradient of hydrophilicity is imposed on a channel wall, the bubble velocity is then decreased; it is most disadvantageous for bubble transport when a bubble moves in a microchannel from a less hydrophilic to a more hydrophilic region. The bubble velocity is affected also by the temperature of the flow field. The surface tension of the methanol–water solution decreases with increasing temperature. The size of a bubble slug in a microchannel is decreased at higher temperature and the mobility of a bubble is increased. We proved also that the Marangoni effect is helpful for bubble transport in a microchannel. Regarding the effect of channel geometry on bubble dynamics, in a convergent microchannel the bubble length is increased as the bubble is gradually compressed on moving toward the outlet of the channel. As the capillary force also increases in a convergent microchannel, the bubble movement is obstructed. If a positive wall temperature gradient (298 K at the inlet to 333 K at the outlet) is imposed, the velocity of bubble transport is significantly increased due to the Marangoni effect. A hydrophilic, divergent channel with a positive wall temperature gradient

is thus favorable for bubble removal in the anode microchannel of a μDMFC.

The thermal lattice-Boltzmann model developed herein is useful for the understanding of the phenomenon of bubble flow in a microchannel. The results also provide important information for the design of the diffusion layer and the flow channel of a μDMFC to avoid blockage by CO_2 bubbles at the anode.

Acknowledgments National Science Council (contract NSC 95-2218-E-007-001) provided financial support; National Center for High-performance Computing provided high-speed computer facilities.

References

Fei K, Hong CW (2007) All-angle removal of CO_2 bubbles from the anode microchannels of a micro fuel cell by lattice-Boltzmann simulation. Microfluid Nanofluid 3:77–88

Fei K, Cheng CH, Hong CW (2006) Lattice Boltzmann simulations of CO_2 bubble dynamics at the anode of a μDMFC. Trans ASME J Fuel Cell Sci Tech 3:180–187

Guo Z, Zheng C, Shi B, Zhao TS (2007) Thermal lattice Boltzmann equation for low Mach number flows: decoupling model. Phys Rev E 75:036704-1-036704-15

Inamuro T, Yoshino M, Inoue H, Mizuno R, Ogino F (2002) A lattice Boltzmann method for a binary miscible fluid mixture and its application to a heat-transfer problem. J Comput Phys 179:201–215

Jun TK, Kim CJ (1998) Valveless pumping using traversing vapor bubbles in microchannels. J Appl Phys 83:5658–5664

Lu GQ, Wang CY (2004) Electrochemical and flow characterization of a direct methanol fuel cell. J Power Sources 134:33–40

Shan X (1997) Simulation of Rayleigh–Bénard convection using a lattice Boltzmann method. Phys Rev E 55:2780–2788

Shan X, Chen H (1993) Lattice Boltzmann model for simulating flows with multiple phases and components. Phys Rev E 47:1815–1819

Shan X, Chen H (1994) Simulation of nonideal gases and liquid–gas phase transitions by the lattice Boltzmann equation. Phys Rev E 49:2941–2948

Shi Y, Zhao TS, Guo ZL (2004) Thermal lattice Bhatnagar–Gross–Krook model for flows with viscous heat dissipation in the impressible limit. Phys Rev E 70:066310-1–066310-10

Takahashi K, Weng JG, Tien CL (1999) Marangoni effect in microbubble systems. Microscale Therm Eng 3:169–182

Takahashi K, Yoshino K, Hatano S, Nagayama K, Asano T (2001) Novel applications of thermally controlled microbubble driving system. Proceedings of the IEEE Micro Electro Mechanical Systems (MEMS) 286–298

Wong CW, Zhao TS, Ye Q, Liu JG (2005) Transient capillary blocking in the flow field of a micro-DMFC and its effect on cell performance. J Electrochem Soc 152:A1600–A1605

Yang H, Zhao TS, Ye Q (2005) In situ visualization study of CO_2 gas bubble behavior in DMFC anode flow fields. J Power Sources 139:79–90

Young T (1805) An essay on the cohesion of fluids. Phil Trans R Soc 95:65–87

Young NO, Goldstein JS, Block MJ (1959) The motion of bubbles in a vertical temperature gradient. J Fluid Mech 6:350–356

Yuan P, Schaefer L (2006a) A thermal lattice Boltzmann two-phase flow model and its application to heat transfer problems-Part 1. Theoretical foundation. Trans ASME J Fluids Eng 128:142–150

Yuan P, Schaefer L (2006b) A thermal lattice Boltzmann two-phase flow model and its application to heat transfer problems-Part 2. Integration and validation. Trans ASME J Fluids Eng 128:151–156